remote sensing

Article

Monitoring Land Subsidence along the Subways in Shanghai on the Basis of Time-Series InSAR

Jinhua Zhang [1,2], Changqing Ke [1,*], Xiaoyi Shen [1], Jinxin Lin [2] and Ru Wang [3]

1 Jiangsu Provincial Key Laboratory of Geographic Information Science and Technology, Key Laboratory for Land Satellite Remote Sensing Applications of Ministry of Natural Resources, School of Geography and Ocean Science, Nanjing University, Nanjing 210023, China
2 Shanghai Institute of Geological Survey, Shanghai 200072, China
3 State Key Laboratory of Information Engineering in Surveying, Mapping and Remote Sensing, Wuhan University, Wuhan 430079, China
* Correspondence: kecq@nju.edu.cn

Abstract: In recent years, Shanghai has entered a stage of microscale land subsidence, but the uneven subsidence is still significant, with long-term impacts on the operational safety of subways and other infrastructures. On the basis of 154 high-resolution Terra Synthetic Aperture Radar-X (TerraSAR-X) images captured from 2013 to 2020 and the time-series persistent scatterer-interferometric SAR (PS-InSAR) method, the land subsidence along the subways in Shanghai was acquired, and the levelling data of 56 benchmarks were used to validate the measurements derived by PS-InSAR. The results indicated that the two data sets agreed well, with a correlation coefficient of 0.9 and maximum D-value of 4.0 mm derived from six pairs of comparative data sequences. The proportion of PS points showing deformation rates between −3.0 mm/a and 3.0 mm/a reached 99.4%. These results indicated that the land subsidence trend along the subway was relatively stable overall, while significant deformation was distributed mainly along the suburban subways, especially the lines that were newly open to traffic, such as Line 5 and the Pujiang line (PJ Line); along these lines, the proportions of PS points with deformation rates exceeding ±3 mm/a were 7.2% and 7.6%, respectively, and the proportions were much smaller in the other lines. The maximum cumulative deformation (MCD) along the subways was located between Jiangchuan Road Station and Xidu Station of Line 5 with a value of −66.4 mm, while the second and third MCDs were −48.2 mm along Line 16 and −44.5 mm along PJ Line, respectively. Engineering constructions, such as human-induced ground loads, foundation pit constructions, and road constructions, were the main factors affecting local land subsidence. The analysis results also showed that land subsidence was relatively significant during the period before the subways were open to traffic due to subway construction, while land subsidence clearly slowed after the subway lines were open to traffic. This deceleration in land subsidence was closely related to the rise in the groundwater level.

Keywords: subways; land subsidence; PS-InSAR; TerraSAR-X; Shanghai

Citation: Zhang, J.; Ke, C.; Shen, X.; Lin, J.; Wang, R. Monitoring Land Subsidence along the Subways in Shanghai on the Basis of Time-Series InSAR. *Remote Sens.* **2023**, *15*, 908. https://doi.org/10.3390/rs15040908

Academic Editor: Deodato Tapete

Received: 9 December 2022
Revised: 20 January 2023
Accepted: 29 January 2023
Published: 6 February 2023

1. Introduction

Land subsidence is a common geological environmental phenomenon that has occurred in at least 150 countries and regions around the world [1,2]. Although land subsidence evolution is irreversible, it is a long and slow natural process in the absence of external-force interference and usually goes unnoticed [3,4]. In recent years, with the rapid development of human society and the accelerating process of urbanization, human activities such as groundwater extraction, ground-surface and underground engineering construction, and mineral mining have greatly aggravated the development of land subsidence, which has evolved into a geological disaster [5–13]. Land subsidence has become a global focus because of its impacts on social development, economic construction, environmental protection, etc. [1,14,15].

In 1921, land subsidence was first noticed in Shanghai, China, through levelling practices [16]. Tracing back the developmental history of land subsidence in Shanghai, land subsidence can be seen to have gone through the evolution process of occurrence–acceleration–rebound–slight subsidence–reacceleration and effective control [1,3,5]. Due to the large amount of groundwater exploited over a long historical period, land subsidence in Shanghai is relatively serious. Since 1921, the maximum deformation magnitude has been close to 3 m, and land subsidence has become the main geological disaster in Shanghai [3,17]. In the 1960s, Shanghai began to control groundwater exploitation and implemented artificial groundwater recharge strategies. Since 2013, the annual groundwater recharge rate has remained above 20 million tons, while groundwater exploitation dropped to 1.18 million tons in 2019, thus effectively mitigating land subsidence [3]. Therefore, land subsidence control in Shanghai has achieved productive results, and the annual deformation rate has decreased to less than −7 mm, marking a new period of microscale deformation [3,5,6]. However, the uneven deformation was still significant, with the large deformation in some regions, and this subsidence directly threatens the urban infrastructures, such as subways, in those regions; in addition, the impact of land subsidence on infrastructure operation safety will last as long as the urban construction activities continue [3,14,18]. Therefore, monitoring land subsidence along subways has great practical significance.

As a new remote sensing technology for ground deformation monitoring, interferometric synthetic aperture radar (InSAR), has the advantages of a short repetition period and high observation accuracy [4,19]. It can effectively overcome the bottleneck problems of traditional monitoring methods, such as sparse observation points, long periods, low efficiencies, and high costs. InSAR has been successfully applied to urban land subsidence monitoring [20,21]. With the launch of high-spatial-resolution and short-period spaceborne SAR systems represented by TerraSAR-X and the COnstellation of small Satellites for the Mediterranean basin Observation (COSMO SkyMed) and the advance of time-series InSAR technologies represented by persistent scatterer (PS) InSAR and small baseline subset (SBAS) InSAR, it has become possible to perform precision deformation monitoring of the deformation of urban infrastructures, such as subways, using InSAR methods [22–26].

In Shanghai, exploration of the application of InSAR technology in land subsidence monitoring began as early as 2004 [27], and some successful cases of these technologies include the application of differential (D)-InSAR, coherent target (CT)-InSAR, PS-InSAR, and SBAS-InSAR to Shanghai land subsidence monitoring [20,21,26–31,33–35]. With the continuous progress and maturity of InSAR technology, in recent years, InSAR technology has also begun to be applied to monitor the deformation of urban infrastructures such as subways and viaducts [18,20,22]. Such technology has also played a positive role in carrying out efficient land subsidence research and ensuring the safety of urban infrastructure operations in Shanghai. At present, it is common to carry out large-scale urban land subsidence monitoring using InSAR methods, while cases of deformation monitoring of specific objects, such as urban infrastructures, are relatively rare; at the same time, research on the characteristics and causes of land subsidence combined with specific objects is also rare.

In this study, high-spatial-resolution TerraSAR-X images captured from 2013 to 2020 were used to retrieve land subsidence information along the subways in Shanghai by time-series PS-InSAR technology, and the deformation results were verified with levelling data. Then, the temporal and spatial evolution characteristics of land subsidence along the subways were analyzed, and the causes of land subsidence were also discussed from the perspectives of the groundwater level, subway construction, and the surrounding environment. This paper provides a reference for understanding the current land subsidence situation along the subways and for conducting targeted prevention and control work under the background of microscale deformation in Shanghai.

2. Study Area and Data

2.1. Study Area

Shanghai is one of the municipalities directly under the Central Government in China and is a core city within the world-class urban agglomeration in the Yangtze River Delta. It is located between 120°52′E and 122°12′E and between 30°40′N and 31°53′N. As a part of the Yangtze River Delta impact plain, the topography of Shanghai is generally lowly inclined from east to west, except for a few hills in the southwest; it is a low and flat plain with an average elevation of 2.19 m and a surface evenness coefficient close to 1 [5,18,36].

By January 2020, the urban rail transit network had taken shape in Shanghai, including 19 rail transit operation lines such as subways, light rails, and maglev trains (Figure 1); 459 operation stations; and 772 kilometers of operational mileage, ranking no. 1 in the world. The maximum daily passenger flow has reached 13.29 million persons-time, accounting for more than 60% of the urban public transport volume [37].

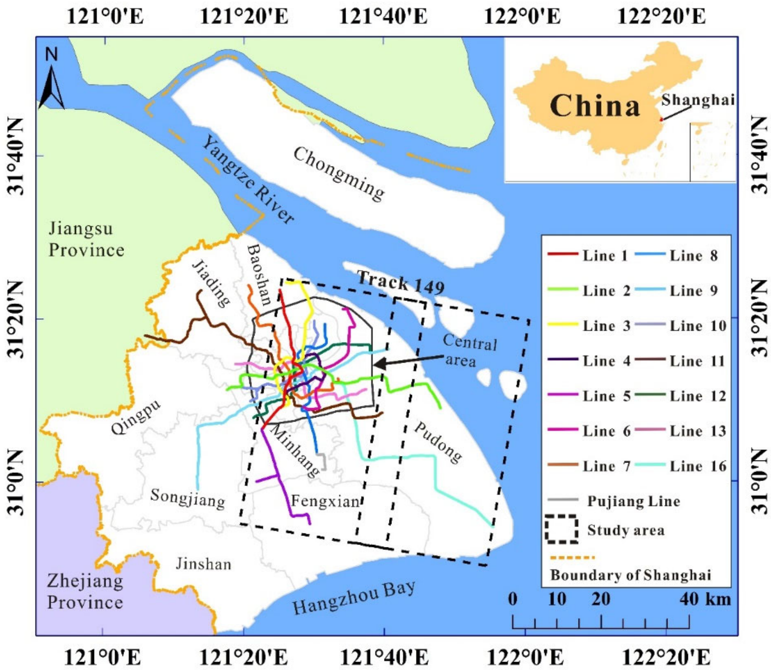

Figure 1. The geographical location of Shanghai, the position of subway lines, and the study area in Shanghai.

2.2. Data

2.2.1. TerraSAR-X Images

TerraSAR-X is the first commercial radar satellite with a resolution of 1 m in the world. The TerraSAR-X satellite adopts a sun-synchronous orbit with an orbital height of 514 km an orbital inclination angle of 97.4°; a repetition period of 11 days; and multiple polarization modes, such as single-polarization, dual-polarization, and full-polarization modes. The TerraSAR-X satellite mainly has three imaging modes: the Spotlight, StripMap, and ScanSAR modes [38].

In this paper, the single-polarization images taken in the strip imaging mode were chosen to select PS targets and generate the deformation field. The spatial resolution of these images was 3 m, and the corresponding land-coverage area of each image was approximately 30 × 50 km^2. Two stacks, including 154 TerraSAR-X images taken from two different image center incidence angles on track 149 (Figure 1), mainly covered areas such as the Shanghai central area, Pudong New Area, Minhang District, Fengxian District, and Baoshan District. The first stack included 76 images, and the image center incidence angle was 39.3° (the west coverage area in Figure 1). The other stacks included 78 images, and the image center incidence angle was 37.8° (the east coverage area in Figure 1). These images were collected from April 2013 to September 2020. Table 1 shows the information of the TerraSAR-X images.

Table 1. Acquisition parameters of TerraSAR-X images.

Track 149							
(Image Center Incidence Angle: 39.3°)				(Image Center Incidence Angle: 37.8°)			
No.	**Acquisition Time**	**Time Baseline**	**Perpendicular Baseline**	**No.**	**Acquisition Time**	**Time Baseline**	**Perpendicular Baseline**
1	20130416	−1309	67.3	1	20130427	−1309	102.4
2	20130508	−1287	38.4	2	20130519	−1287	40.2
3	20130530	−1265	140.4	3	20130610	−1265	98.6
4	20130621	−1243	95.0	4	20130702	−1243	−82.5
5	20130713	−1221	−99.6	5	20130724	−1221	155.0
6	20130804	−1199	97.3	6	20130815	−1199	−173.3
7	20130826	−1177	50.2	7	20130928	−1155	57.1
8	20130917	−1155	28.2	8	20131111	−1111	−174.0
9	20131009	−1133	−237.5	9	20131203	−1089	66.1
10	20131122	−1089	−60.2	10	20131225	−1067	52.2
11	20131214	−1067	−69.4	11	20140105	−1056	64.8
12	20140312	−979	18.6	12	20140323	−979	21.5
13	20140517	−913	92.6	13	20140528	−913	256.8
14	20140711	−858	87.4	14	20140630	−880	125.6
15	20140802	−836	77.0	15	20140722	−858	210.0
16	20140824	−814	144.1	16	20140813	−836	137.0
17	20140915	−792	168.3	17	20140904	−814	57.1
18	20141007	−770	−97.6	18	20140926	−792	40.6
19	20141029	−748	−6.4	19	20141018	−770	−34.2
20	20141201	−715	121.4	20	20141109	−748	39.0
21	20141223	−693	78.1	21	20141212	−715	144.1
22	20150310	−616	375.6	22	20150216	−649	197.0
23	20150401	−594	34.6	23	20150504	−572	105.0
24	20150515	−550	28.8	24	20150606	−539	35.5
25	20150617	−517	67.7	25	20150709	−506	−9.9
26	20150822	−451	−62.0	26	20150811	−473	63.7
27	20150924	−418	−49.3	27	20151016	−407	30.2
28	20151027	−385	28.1	28	20151210	−352	100.7
29	20151221	−330	125.3	29	20160101	−330	62.2
30	20160329	−231	25.4	30	20160203	−297	−31.6
31	20160501	−198	93.5	31	20160409	−231	181.9
32	20160603	−165	243.3	32	20160512	−198	124.9
33	20160706	−132	185.7	33	20160614	−165	183.3
34	20160808	−99	64.1	34	20160717	−132	49.8
35	20160910	−66	91.0	35	20160819	−99	195.8
36	20161013	−33	−74.0	36	20160921	−66	80.6
37	20161115	0	0.0	37	20161024	−33	83.3
38	20161218	33	115.0	38	20161126	0	0.0
39	20170120	66	−27.2	39	20161229	33	230.5
40	20170305	110	−101.2	40	20170131	66	74.1
41	20170407	143	131.3	41	20170316	110	−96.8
42	20170429	165	31.7	42	20170418	143	−101.0
43	20170521	187	−54.5	43	20170510	165	88.0
44	20170612	209	−54.1	44	20170601	187	15.9
45	20170704	231	76.3	45	20170623	209	169.0

Table 1. *Cont.*

Track 149							
(Image Center Incidence Angle: 39.3°)				(Image Center Incidence Angle: 37.8°)			
No.	Acquisition Time	Time Baseline	Perpendicular Baseline	No.	Acquisition Time	Time Baseline	Perpendicular Baseline
46	20170726	253	−32.4	46	20170715	231	92.0
47	20170908	297	−20.8	47	20170806	253	95.5
48	20170930	319	−403.4	48	20171011	319	−255.3
49	20171022	341	84.3	49	20171102	341	−159.4
50	20180303	473	82.8	50	20180220	451	−128.3
51	20180405	506	−319.6	51	20180325	484	169.3
52	20180508	539	−133.5	52	20180427	517	188.1
53	20180621	583	−136.5	53	20180610	561	−348.2
54	20180804	627	−163.6	54	20180713	594	−81.5
55	20180917	671	26.4	55	20180826	638	−136.1
56	20181111	726	−328.7	56	20181009	682	199.7
57	20181203	748	−446.3	57	20181122	726	150.4
58	20190116	792	−289.3	58	20190105	770	36.5
59	20190207	814	177.8	59	20190218	814	211.4
60	20190301	836	−360.5	60	20190312	836	19.5
61	20190323	858	−165.8	61	20190403	858	−310.0
62	20190506	902	79.9	62	20190517	902	89.8
63	20190528	924	−48.0	63	20190608	924	−386.4
64	20190619	946	−167.2	64	20190802	979	2.0
65	20190824	1012	−406.7	65	20190904	1012	52.1
66	20191029	1078	−40.5	66	20190926	1034	−311.0
67	20191120	1100	−155.8	67	20191018	1056	157.6
68	20191212	1122	−21.4	68	20191109	1078	−11.3
69	20200114	1155	138.5	69	20191201	1100	−57.6
70	20200320	1221	−107.4	70	20191223	1122	−184.1
71	20200525	1287	106.9	71	20200125	1155	19.6
72	20200616	1309	63.3	72	20200216	1177	−75.6
73	20200708	1331	101.1	73	20200309	1199	−111.1
74	20200730	1353	−503.3	74	20200514	1265	−32.4
75	20200821	1375	−405.3	75	20200627	1309	−439.9
76	20200901	1386	107.5	76	20200719	1331	−353.1
				77	20200810	1353	−12.1
				78	20200912	1386	−365.3

2.2.2. Geological Environment Data

Data were collected from 56 benchmarks and 3 groundwater wells along the subways (Figure 2). The elevation data of the benchmarks, which are required to be collected by the manual levelling method with an accuracy of ±2 mm once a year, usually between August and October, were used to verify the accuracy of the land subsidence results measured by time-series InSAR methods. The groundwater level data, which were required by manual measurements with an accuracy of ± 1 cm once a month, were used to analyze the land subsidence characteristics along the subways. All these data were provided by the Shanghai Institute of Geological Survey.

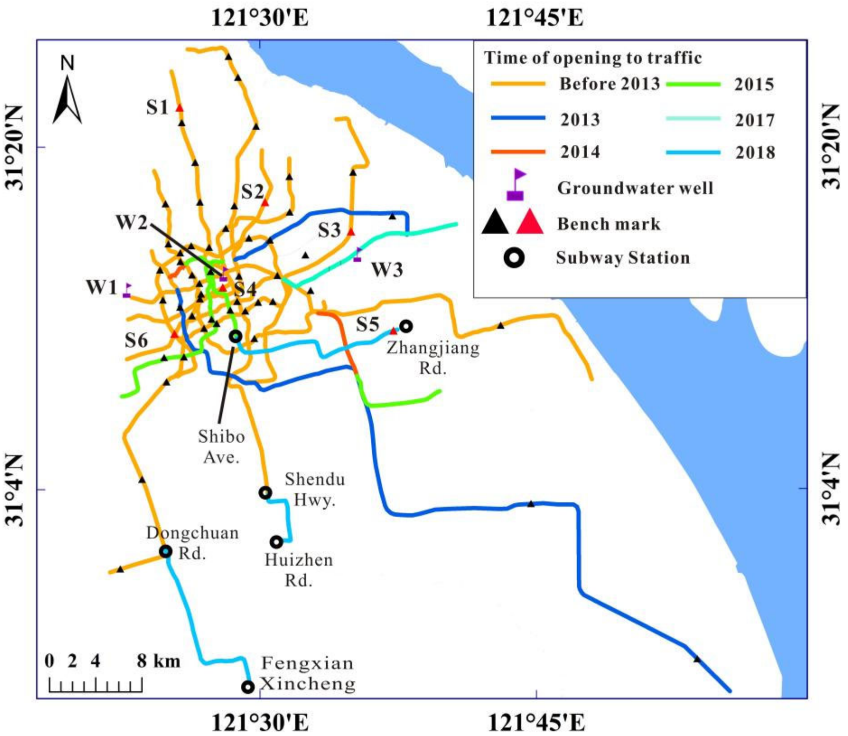

Figure 2. The distribution of the subway lines with different times of opening to traffic, the benchmarks, and the groundwater wells in the study area.

2.2.3. Optical Images

Optical images were taken by aerial photography with DMC2001 or DMCIII cameras once a year, usually in the first half of the year, and the resolution was better than 0.25 m. These images were used mainly to extract the ground-environment variations along the subways, such as variations resulting from engineering construction and land use; these variations were thought to be conducive to further analyses of the characteristics and causes of land subsidence. These optical images were provided by the Shanghai Surveying and Mapping Institute.

3. Methodology

3.1. Principle of Time-Series PS-InSAR

In 1999, the PS-InSAR method was first proposed by [39] in Italy. The basic principle was to select PSs that could maintain stable coherence under the temporally and spatially long baselines of multiple SAR images. These PS points were distributed mainly on artificial buildings, exposed rocks, etc. The surface deformation information was obtained through PS network modelling and solving. This method could truly achieve surface deformation information at a millimeter-level accuracy using PS-InSAR approaches due to the strong coherence of the PS points, thus greatly reducing the impacts of temporal and spatial incoherence on the quality of the interferometric phase [30,31,40,41].

3.2. Data Processing

An image among N + 1 single-complex SAR images was chosen as the main image, and the other images were combined with the main image to form N SAR interferograms. After removing the flat ground phase and terrain phase, the differential phase of the PS points in the *i*th differential interferogram could be expressed as follows:

$$\Phi_{diff} = \Phi_{def} + \Phi_{topo-e} + \Phi_{orb} + \Phi_{atm} + \Phi_{noise} \quad (1)$$

where Φ_{def} is the deformation phase due to surface movement along the satellite line-of-sight (LOS) direction; Φ_{topo-e} is the residual topographic phase due to DEM errors; Φ_{orb} is the residual phase due to satellite orbit inaccuracies; Φ_{atm} is the atmospheric phase due to atmospheric delay; and Φ_{noise} is the noise phase due to multiple factors, such as thermal noise, scattering variability, and registration errors.

In this study, the main image was selected by maximizing the total coherence coefficient of all interferograms ($\max(\sum_{i=1}^{N} \gamma_{total}^{i})$). The term γ_{total} is composed mainly of the temporal coherence $\gamma_{temporal}$, spatial coherence $\gamma_{spatial}$, Doppler coherence $\gamma_{doppler}$, and thermal noise coherence γ_{themal} (Equation (2)):

$$\begin{aligned} \gamma_{total} &= \gamma_{temporal} \times \gamma_{spatial} \times \gamma_{doppler} \times \gamma_{themal} \\ &\approx \left(1 - f\left(\frac{T}{T^c}\right)\right) \times \left(1 - f\left(\frac{B_\perp}{B_\perp^c}\right)\right) \times \left(1 - f\left(\frac{F_{DC}}{F_{DC}^c}\right)\right) \times \gamma_{themal} \\ & f(x) = \left\{ \begin{matrix} x, & x \le 1 \\ 1, & x > 1 \end{matrix} \right\} \end{aligned} \quad (2)$$

where T, $B_\perp$, and F_{DC} represent the temporal baseline, perpendicular baseline, and Doppler frequency difference of the interference pair, respectively, and T^c, $B_\perp^c$, and F_{DC}^c represent the corresponding critical values. For the TerraSAR-X data, the critical values are 500 d, 1605 m, and 800 Hz, respectively [30,31].

On the basis of the main image selection methods above, the images taken on 15 November 2016 (image center incidence angle: 39.3°) and 26 November 2016 (image center incidence angle: 37.8°) were selected as the main images. Figure 3 shows the temporal and perpendicular baselines of the interference image pairs.

According to the data processing flow chart, showed in Figure 4. The whole process could be simplified into 3 steps. First, PS points were selected through iteration of binning PS candidates by amplitude and gamma, normalizing gamma distribution of random pixels and fitting of the gamma threshold line for PS candidates [32]. The gamma threshold is actually determined by each pixel. In addition, the default value is 0.3; then, the phase gradient between adjacent PS points was calculated with the Delaunay irregular triangular network. Second, the linear deformation rate and elevation residual of each PS point were obtained on the basis of the three-dimensional phase-unwrapping algorithm. Finally, the residual phases, such as the atmospheric phase, orbital phase, nonlinear deformation phase, and noise phase, were separated and estimated by spatiotemporal filtering methods applied to obtain more accurate deformation results. Some key parameter settings of PS-InSAR were listed as follows (see Table 2):

Table 2. Key parameter settings of PS-InSAR.

Parameter Name	Value
Amplitude dispersion index	0.3
Weed_max_noise	1.5
Weed_standard_dev	1.2
Unwrap_method	'3D_quick'
Unwrap_grid_size	60
Max_topo_err	30

Due to the relative deformation obtained in each coverage area, it is necessary to integrate the data of these two coverages to obtain a whole deformation information based on the same reference frame. Similar to the method used in the previous research [33], the west coverage area was chosen as the master scene and the east coverage area was transformed to the master scene through the common points in the overlapping area. Then, the average offset between the two coverages was calculated, which used to update the data of the east coverage area. On the basis of the data in master scene and the updated data in the other scene, the average value was calculated as the ultimate velocity of the points in the overlapping area. In this way, the integrated deformation velocity in the whole area was available. Finally, the PS points were extracted from the region of 50 m on both sides of the subway line to characterize the ground deformation along the subways.

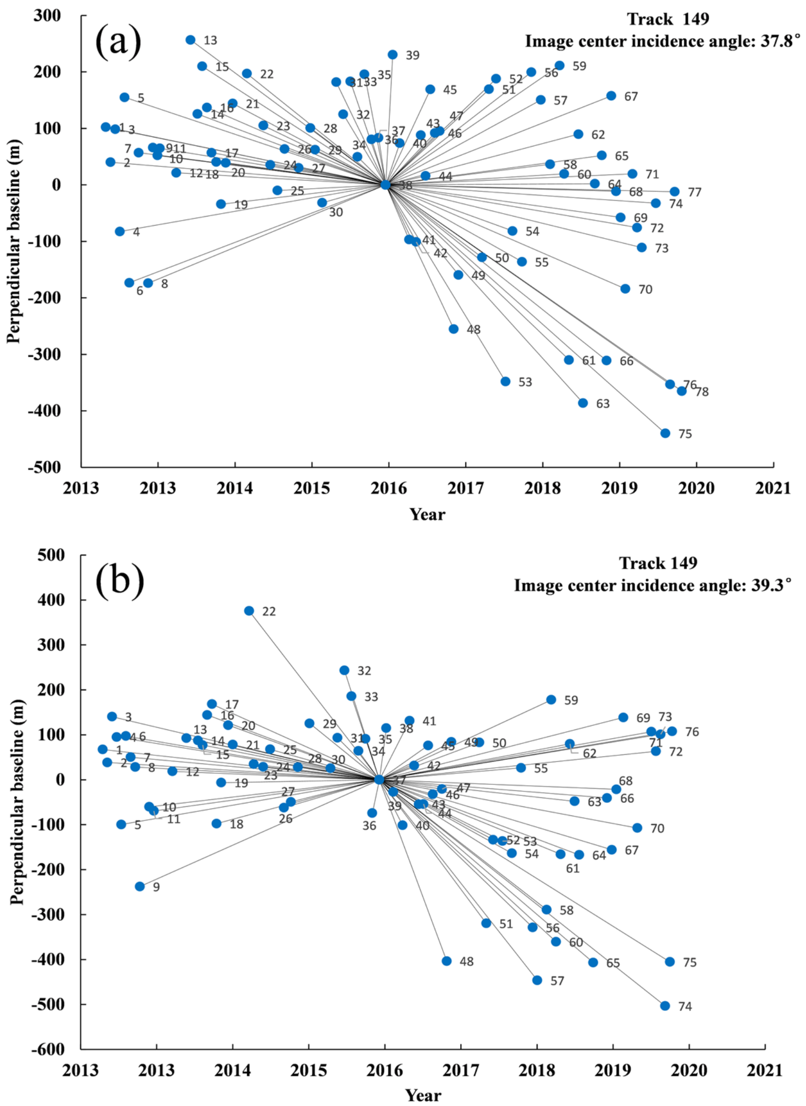

Figure 3. The perpendicular and temporal baselines of TerraSAR-X interferometric image pairs; the blue points represent the SAR images and the black lines represent the interferogram. (**a**) shows the temporal and perpendicular baselines of the interference image pairs (image center incidence angle: 37.8°), (**b**) shows the temporal and perpendicular baselines of the interference image pairs (image center incidence angle: 39.3°).

The accuracy of PS-InSAR results is mainly obtained by comparing them with high-precision levelling data. It is acceptable that the standard deviation of these two data sets is less than ±5 mm/a [30,35,40–42].

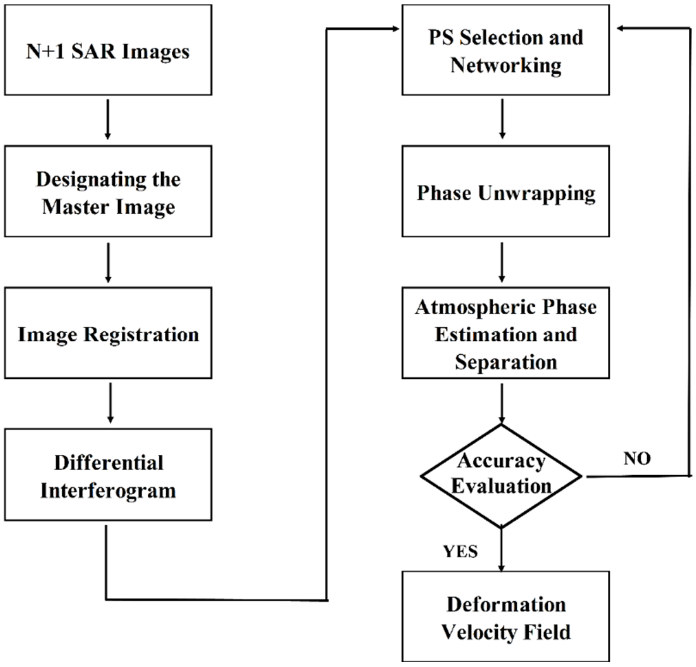

Figure 4. The diagram of data processing with PS-InSAR.

4. Results

4.1. Verification

According to the locations of 56 benchmarks along the Shanghai Metro lines (Figure 2), the average value of all the PS points' monitoring results obtained by InSAR methods within 50 m around each benchmark was calculated. Then, a correlation analysis was performed between the two data sets. The results (Figure 5) showed a correlation coefficient of 0.9 and standard deviation of $\pm$ 0.4 mm/a, indicating that the deformation rates derived by levelling and InSAR were well correlated.

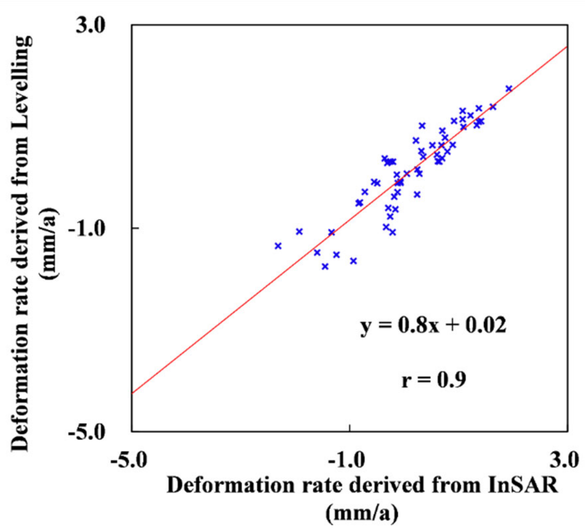

Figure 5. Comparison of the ground deformation rates derived from InSAR and levelling.

To further confirm the accuracy of the time-series InSAR monitoring results, six benchmarks, S1–S6, were selected from 56 benchmarks according to the principle of uniform location distribution (Figure 2), and the annual benchmark monitoring data series from 2013 to 2020 were compared with the time series formed with the average value of PS points within approximately 50 m. Figure 6 shows that the time series of the two data sets were well correlated overall. Forty-two groups of comparison data were obtained, excluding the initial comparison data in 2013 (the initial value of which was 0), and the proportion reached 86% with a D-value less than 3.0 mm; in addition, only six groups' D-values were greater than 3.0 mm, and the maximum D-value was 4.0 mm. There were two main reasons for the difference in the data groups: ① the systematic error of the two measurement methods, the levelling, and PS-InSAR methods, and ② the benchmark data represented the deformation of a specific point, while the InSAR monitoring data represented the average deformation of the area within approximately 50 m.

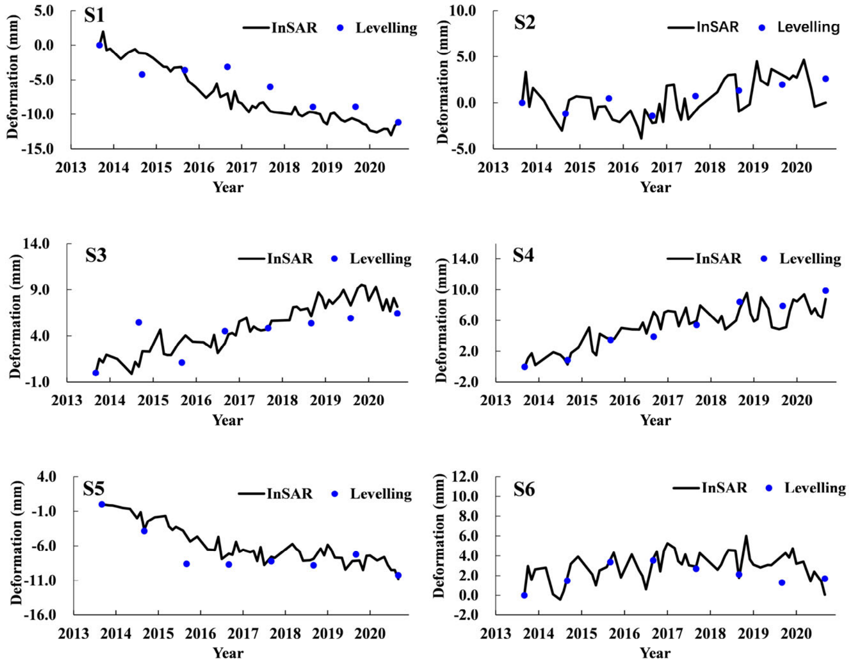

Figure 6. Time series of ground deformation data derived from InSAR and levelling between 2013 and 2020. Plots (**S1**–**S6**) shows the comparison of deformation time-series derived from InSAR and the corresponding levelling measurements at the six available levelling benchmarks, labeled as **S1**, **S2**, **S3**, **S4**, **S5**, **S6**.

In conclusion, the ground deformation information derived from the time-series InSAR data in this study was reliable and accurate.

4.2. Spatial Distribution Characteristics of Ground Deformation

The ground deformation along the subways remained stable in general from 2013 to 2020 (Figure 7), and the deformation rates of 99.4% of the PS points were between −3.0 mm/a and 3.0 mm/a, mainly concentrated in the Shanghai central area. These results agreed with the microscale deformation of Shanghai in recent years [3,5,6]. From the perspective of the ground deformation trend, 69% of the PS points showed upwards rebounds, and the maximum ascent rate was approximately 3.7 mm/a, indicating that the ground deformation along the subways in general was in a slight ascending stage from 2013 to 2020.

The areas with relatively severe land subsidence were distributed mainly in the suburbs, especially along the newly operated subways, such as Line 5 and the Pujiang Line (PJ Line), which were opened to traffic in 2018. As shown in Figure 8, the PS points with deformation rates larger than ± 3.0 mm/a accounted for 7.2% of all PS points along Line 5, while this percentage was 7.6% along the PJ Line. Among the other lines, Line 11 had the highest proportion at 2.2%, followed by Line 10 with a proportion of 1.2%. The proportions of the remaining lines were all less than 1%, and Line 4 had the lowest proportion of only 0.08%, indicating that land subsidence was easier to develop along the newly operated lines. Regarding the cumulative deformation from April 2013 to September 2020, the maximum cumulative deformation (MCD) among all lines was located between Jiangchuan Road Station and Xidu Station (Q2) along Line 5 with a value of −66.4 mm (deformation rate: −8.9 mm/a), and the MCD along the PJ Line was −44.5 mm (deformation rate: −6.0 mm/a), located between Sanlv Road Station and Shendu Road Station (Q1). In addition, a subsidence funnel was observed between Wangyuan Road Station and Jinhaihu Station (F) along Line 5, the MCD of which was −40.8 mm (deformation rate: −5.5 mm/a). Among the other lines, the MCDs of Line 16, Line 11, and Line 9 were −48.0 mm, −41.5 mm, and −41.5 mm, respectively, while the MCDs of the remaining lines were all less than −40 mm and the MCD of Line 7 was only −26.0 mm, the minimum MCD among all lines. The MCD comparison results indicated that land subsidence was relatively severe along the newly operated lines. These results were consistent with those of [18,22].

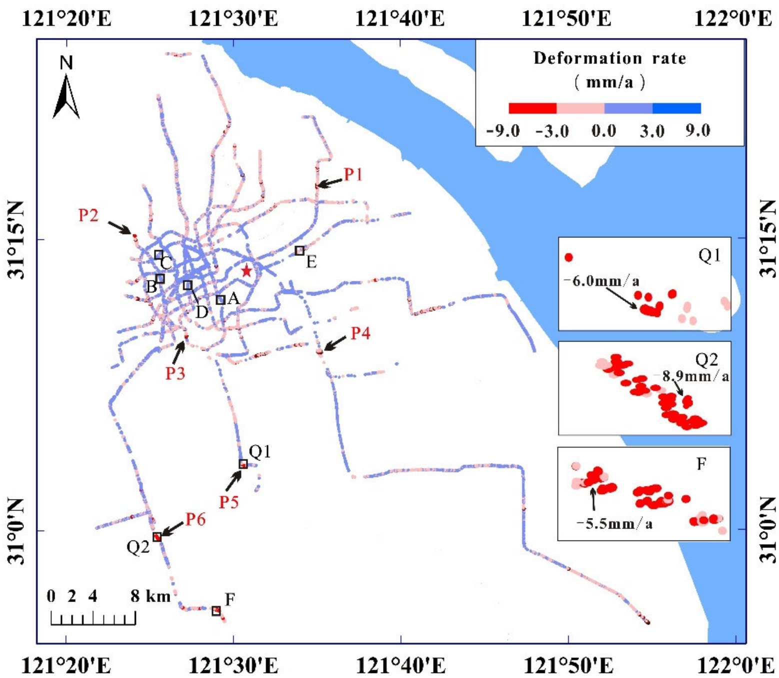

Figure 7. The ground deformation rate along the subways in Shanghai derived from InSAR between 2013 and 2020. The red five-pointed star represents the position of the reference point.

Although subsidence funnels were observed along almost every line, such funnels were scattered individually with a small scope and contributed little to the overall land subsidence characteristics along the subway lines.

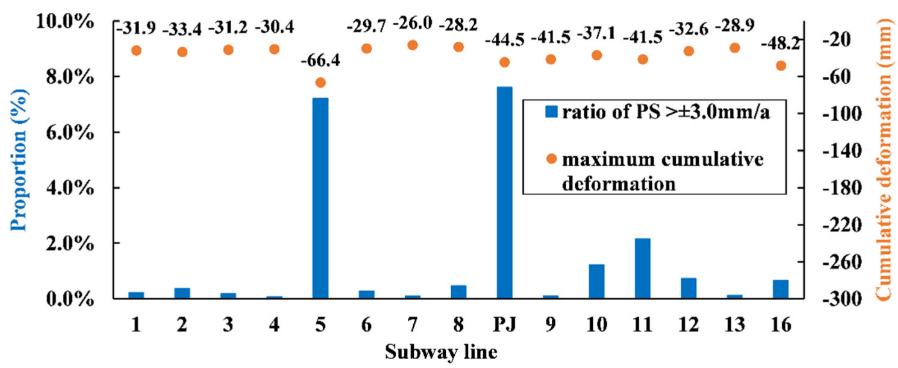

Figure 8. Proportion of PS points (>±3.0 mm/a) and maximum cumulative deformation along subway lines from 2013 to 2020.

4.3. Temporal Evolution Characteristics of Land Subsidence

In the study area, Line 1 was the first subway to be opened to traffic, opening in 1993, while the last lines were the section between Dongchuan Road Station and Fengxian Xincheng Station along Line 5, the section between Shendu Highway Station and Huizhen Road Station along the PL Line, and the section between Shibo Avenue Station and Zhangjiang Station; these sections were opened to traffic in 2018. Most of the other subway lines were opened to traffic before 2013 (Figure 2). No subway lines were opened to traffic in 2016 or 2019.

To ensure the reliability and objectivity of the analysis results to the greatest possible extent, according to the different years the subway lines opened to traffic, PS points were selected in six representative areas labelled A-F (Figure 2) *without other engineering constructions,* and the average value of all the PS points' monitoring results in each zone was calculated to represent the regional ground deformation. Through the regional ground deformation time-series, we aimed to study the temporal evolution characteristics of land subsidence along the subway lines before and after opening to traffic. As shown in Figure 9, Zone A was located between the China Art Museum Station and South Xizang Road Station along Line 8, which was opened to traffic in December 2007. From 2013 to 2015, the ground deformation of Zone A exhibited uplift overall, with a maximum value of approximately 9 mm. From 2015 to 2020, the ground deformation fluctuated around a height of 9 mm, and the deformation trend was relatively stable. Zone B was located between Jiangsu Road Station and Jiaotong University Station along Line 11, which was opened to traffic in August 2013. In the first half of 2013, the land subsidence of Zone A was approximately −2.8 mm; then, this zone began to rebound upwards until 2017. From 2017 to 2020, the ground deformation fluctuated around a height of 6.5 mm. Zone C was located between Wuning Road Station and Changshou Road Station along Line 13, which opened to traffic in December 2014. In 2013, the PS points of Zone C subsided slightly by approximately −1 mm. From 2014 to 2016, the ground began to rebound upwards gradually, while from 2016 to 2020, the rebound rate was significantly accelerated, with a total upwards deformation of approximately 5 mm. Zone D was located between Jiashan Road Station and Damuqiao Road Station along Line 12, which opened to traffic in December 2015. From 2013 to 2017, the land subsidence of Zone D was approximately −15 mm, while from 2017 to 2020, the land subsidence rate slowed down significantly, with a total subsidence of only approximately −5 mm. Zone E was located between Lantian Road Station and Fangdian Road Station along Line 9, which opened to traffic in December 2017. The land subsidence of Zone E was approximately −2.5 mm from 2013 to 2017, while the ground rebounded upwards gradually from 2017 to 2020, with a total rebound amplitude of approximately 3.8 mm. Zone F was located between Wangyuan Road Station and Jinhai Road Station along Line 5, which opened to traffic in December 2018. From 2013 to 2014, the ground uplifted slightly by approximately 10 mm, while after a short period of stability in 2014, the ground subsided quickly with a total deformation of approximately −12 mm from 2015 to 2018. In the last two years, the ground subsidence slowed down significantly and fluctuated around a height of −12 mm.

On the basis of the analysis results presented above, except for Zone A, where the subway line opened to traffic earlier than 2013, land subsidence was clearly observed before the other five areas opened to traffic, and the deformation trends changed significantly after these sections opened to traffic, e.g., the deformation eased or rebounded upwards, indicating that the timing when such zones opened to traffic was an important moment in the evolution of land subsidence along the subways, *although the time of opening to traffic was not completely consistent with the change time of land subsidence trend.* The reasons for the inconsistency between these two temporal nodes were mainly that two deformation stages occurred before the subway lines opened to traffic: the subway construction and post-construction deformation stages. If the subway constructions were completed late, the post-construction deformation continued after the subway was opened to traffic, and vice versa, if constructed ended prematurely, post-construction deformation may have also ceased before the subway was open to traffic.

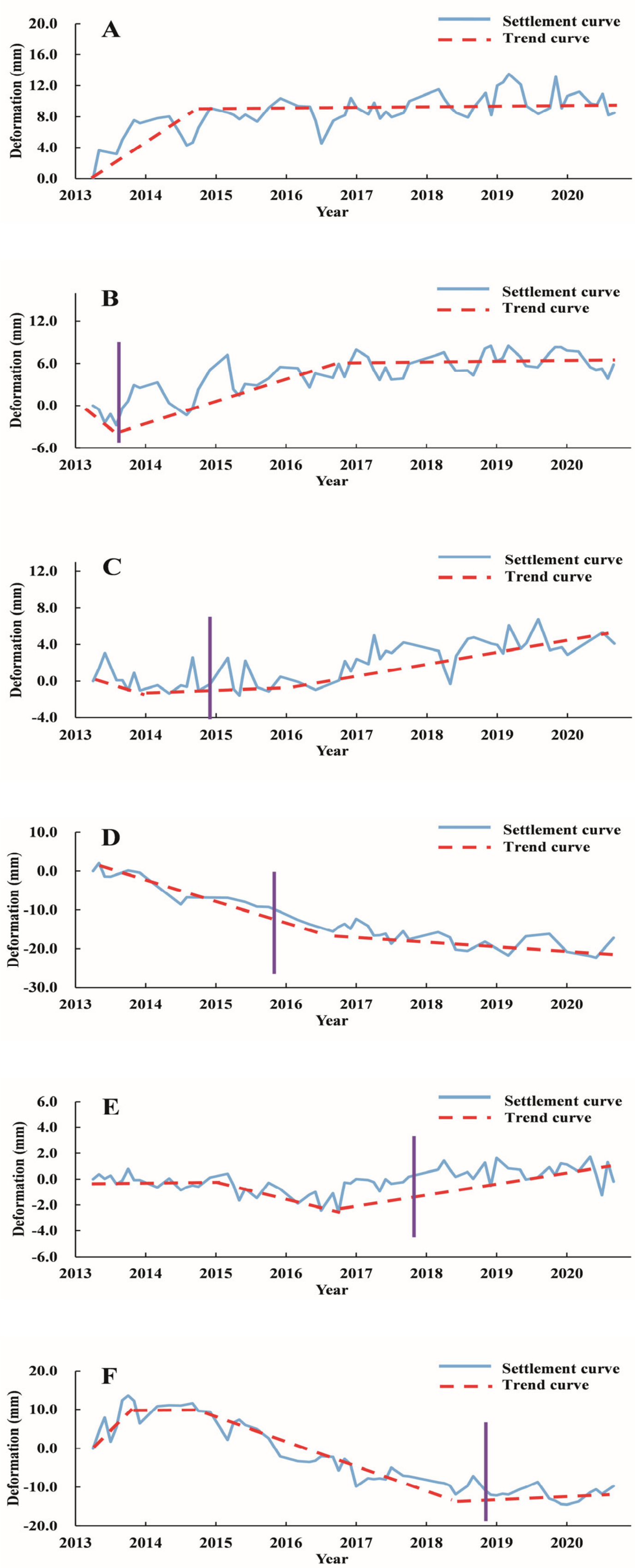

Figure 9. Curve of time series ground deformation along the subways in Shanghai from 2013 to 2020 (purple lines represent the time of opening to traffic). Plots (**A**–**F**) shows the ground deformation characteristics respectively in the six areas, labeled as **A**, **B**, **C**, **D**, **E**, **F**.

In addition, after the subway was opened to traffic, the ground rebound was all observed, except for Zone D. The ground rebound was most likely related to the strict control of groundwater exploitation and massive recharge of groundwater in Shanghai, which is discussed in detail in Section 5.2. The reason for the fact that the ground rebound did not occur in Zone D might be that inelastic deformation was dominant in the development of land subsidence [41], that is, the ground will not rebound as the groundwater level rises.

5. Discussion

5.1. Impact of Engineering Construction

Variations in the surrounding environment were commonly observed in the areas with relatively severe land subsidence along the subways, and six representative cases, labelled as P1–P6 (Figure 7), were selected for further analysis.

From the aerial images (Figure 10), extensive engineering constructions were obviously observed in the four areas of P1, P2, P3, and P4. The ground subsided continuously during the period of foundation pit construction in P1 and P2, spanning from 2013 to 2017. When the main building constructions were almost completed in 2017, the ground deformation subsequently decelerated significantly. Unlike P1 and P2, land subsidence continued to intensify in P3 from 2013 to 2020 due to the continuous implementation of foundation pit construction. Regular fluctuations were observed in the continuous deformation process, which may have been related to fluctuations in the groundwater level. In the case of P4, Luoshan Elevated Interchange, Lines 11 and Line 16 were constructed from 2013 to 2017; later, foundation pit construction work was carried out from 2017 to 2020, which led to the result that the land subsidence trend was not alleviated all the time. P5 was the location of a subway garage, and 2013–2017 was the period of garage construction. After 2017, the ground load caused by subway trains parking on the track and in the garage was the main reason for the continuous ground deformation observed in this area. The ground load caused by the long-term stacking of large quantities of concrete and other construction materials was related to the continuous land subsidence due to the concrete manufacturing companies being located in P6.

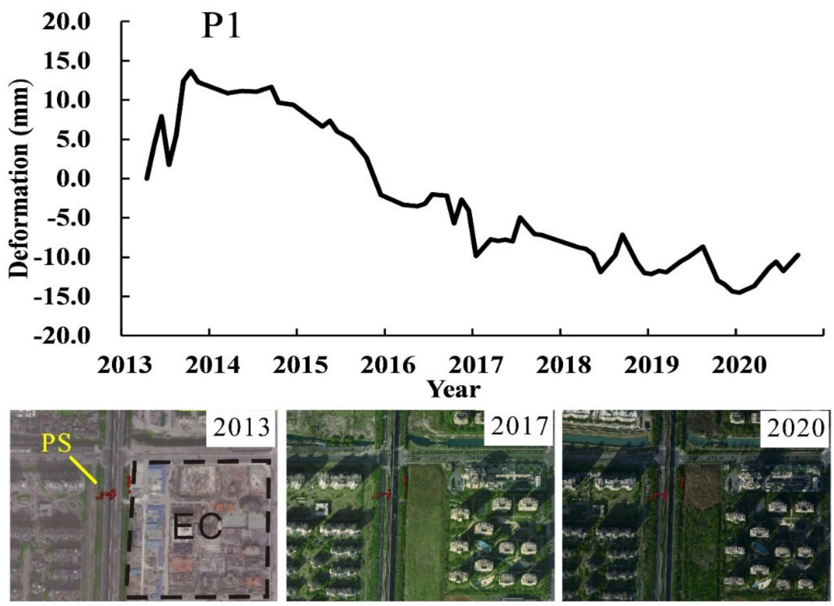

Figure 10. *Cont.*

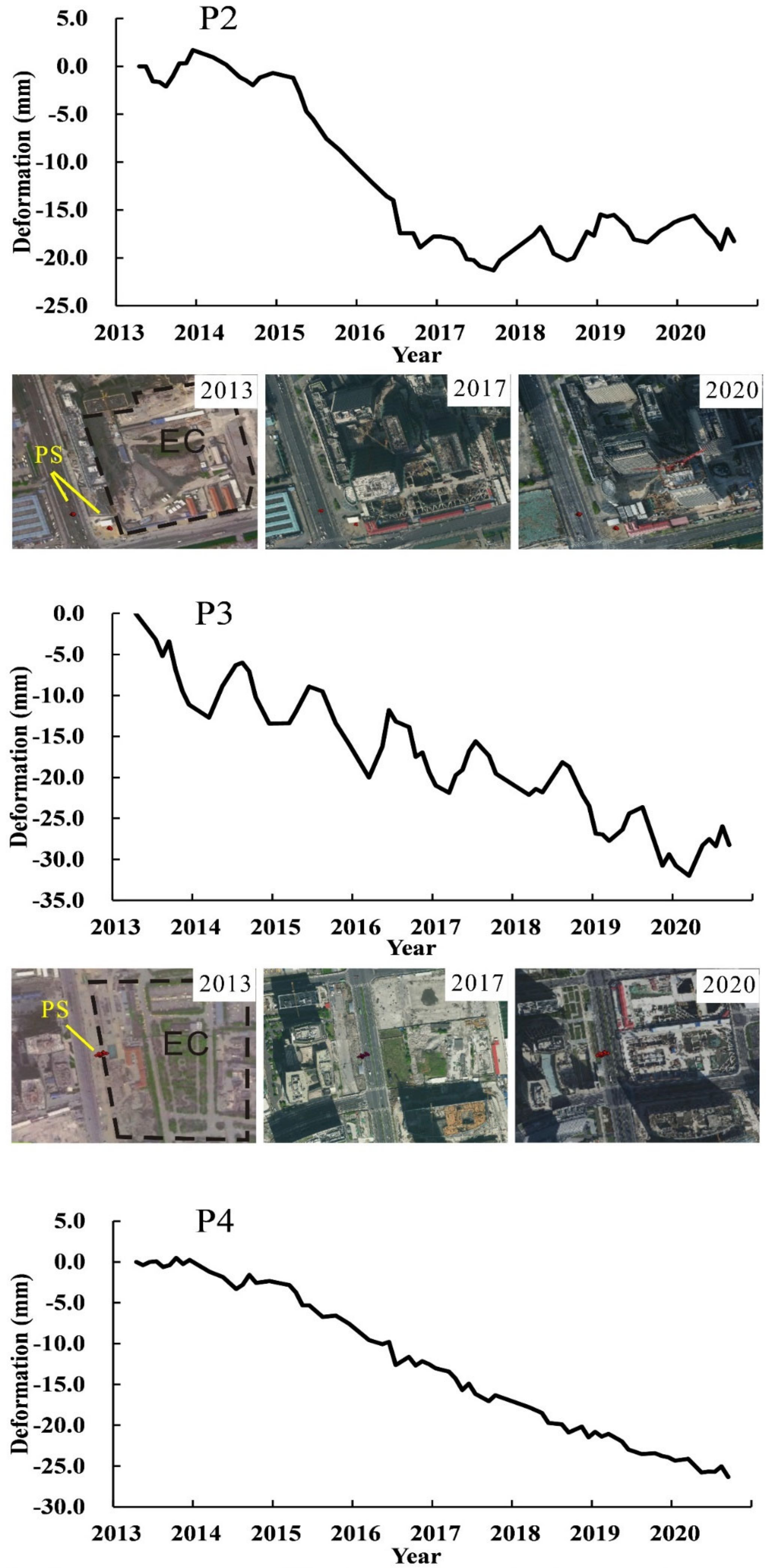

Figure 10. *Cont*.

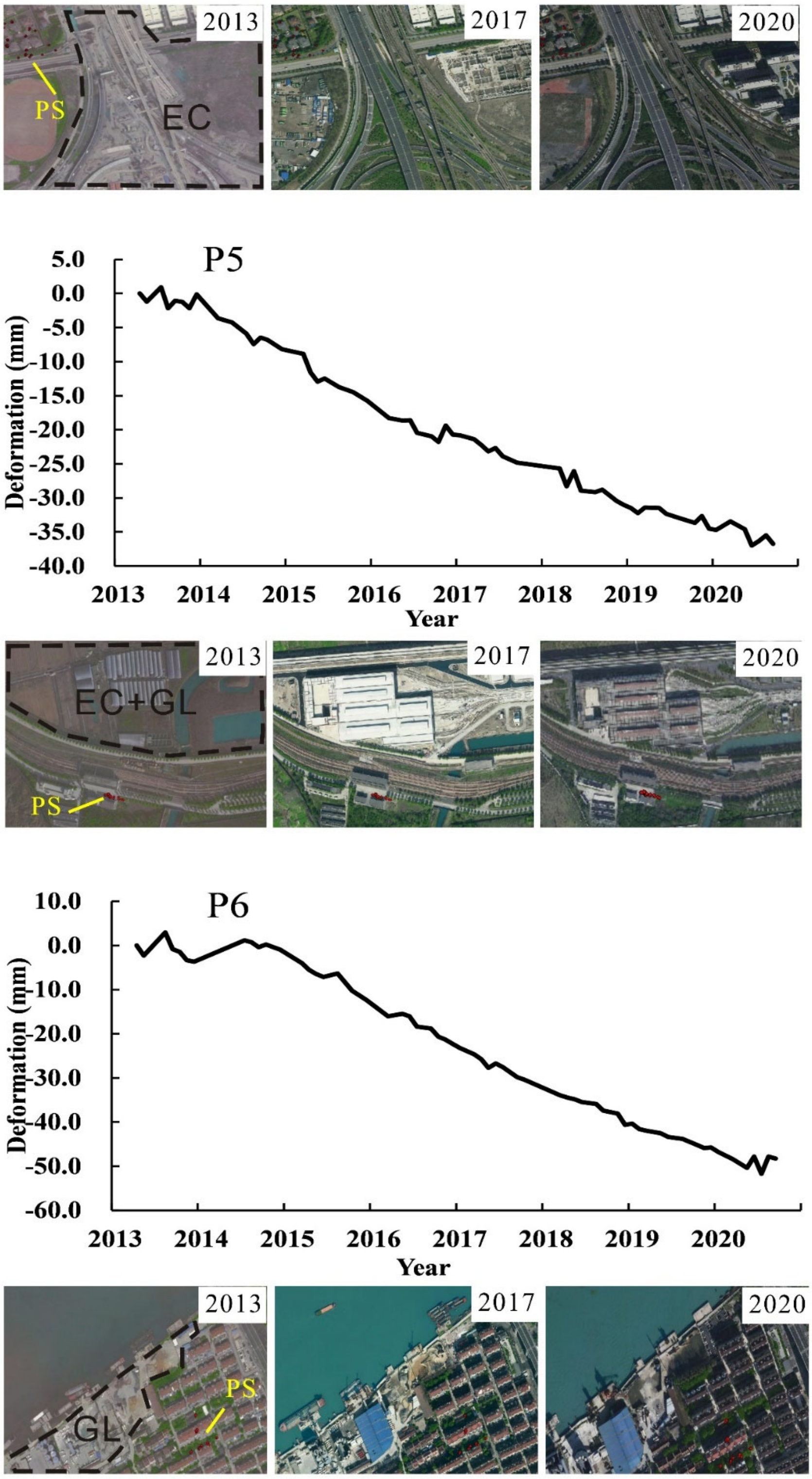

Figure 10. Curve of time series ground deformation and aerial images of the surrounding land cover change (EC: engineering construction, GL: ground load). Plots (**P1**–**P6**) shows the ground deformation and the corresponding aerial images respectively in the six areas, labeled as **P1**, **P2**, **P3**, **P4**, **P5**, **P6**.

In the process of engineering constructions, it is often accompanied by soil disturbance and foundation pit dewatering, which are the main reasons for inducing the surrounding land subsidence. In addition, the constructed buildingsand roads, the parked subway *trains, and concrete materials (P6) mentioned aboveincreased the surface load, leading to soil consolidation and contributing to land subsidence.*

In conclusion, engineering constructions, such as human-induced ground loads, foundation pit construction, and road construction, were the main reasons affecting land subsidence intensification.

5.2. Impact of the Groundwater Level

The groundwater level is closely related to land subsidence, and the massive exploitation of groundwater is considered to be the main reason for land subsidence [2,5,7,10,42,43]. To analyze the correlation between groundwater level and land subsidence, the average value of all the PS points' monitoring results within 500 m around the ground water wells, such as W1, W2, and W3, was calculated to represent the regional land subsidence. Figure 11 shows the time sequences of the groundwater level and land subsidence with the unit of the well positions, and the correlation coefficients were calculated as 0.725 for W1, 0.840 for W2, and 0.830 for W3, indicating that the groundwater level and surrounding land subsidence were significantly positively correlated. These results were consistent with those of [6,18]. The correlation coefficient of W1 was relatively low, and the main reason for this result may have been that the number of PS points was not sufficient to fully reflect the land subsidence around W1 due to the location of the well being outside the study area (Figure 2).

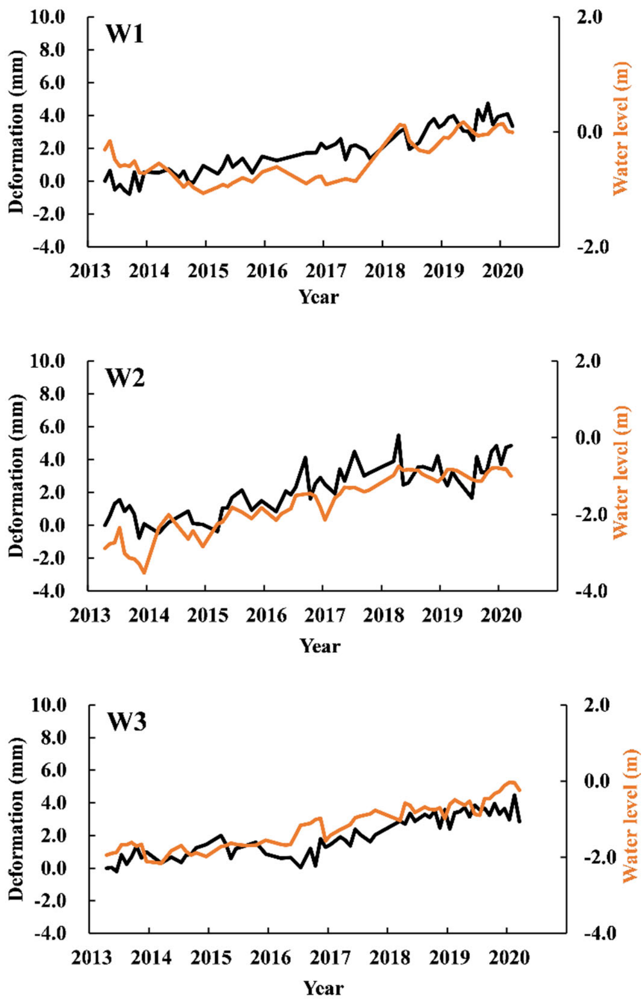

Figure 11. Curve of time series groundwater level and ground deformation in Shanghai from 2013 to 2020. Plots (**W1**–**W3**) shows the groundwater level and the corresponding ground deformation respectively around the three wells, labeled as **W1**, **W2**, **W3**.

As shown in Figure 11, the ground deformation around the wells was small and followed the process from micro-subsidence to micro-upward rebound, accompanied by an increase in the groundwater level. It was likely that elastic deformation occurred in the aquifer around the wells [43], that is, the ground will slowly rebound as the groundwater level rises.

This phenomenon was mainly related to the strict control of groundwater exploitation in Shanghai. Since 2011, the annual groundwater recharge has exceeded the groundwater exploitation, and the ratio of the quantities of recharged and exploited water reached 17:1 in 2020 [44].

6. Conclusions

On the basis of TerraSAR-X images and time-series PS-InSAR technology, land subsidence information along the subways in Shanghai from 2013 to 2020 was acquired and verified with levelling data from benchmarks. Through the analysis of the spatiotemporal distribution characteristics and influencing factors of land subsidence, the following conclusions were obtained:

(1) The comparison results of the annual deformation rate derived by time-series InSAR and levelling demonstrated that the two data sets were well correlated with a correlation coefficient of 0.9 and a standard deviation of $\pm$0.4 mm; in addition, the deformation time series measured by these two methods also agreed well, with a maximum D-value of 4.0 mm derived from 42 pairs of comparative data. Thus, the ground deformation information acquired from time-series InSAR was both accurate and reliable.

(2) From 2013 to 2020, the ground deformation trend along the subways in Shanghai was generally stable, exhibiting microscale upwards rebound overall. Areas of significant deformation were distributed mainly along the suburban subways, especially the lines that were newly open to traffic, such as Line 5 and the PJ Line, with maximum cumulative deformation magnitudes of -66.4 mm and -44.5 mm, respectively. It was also observed that the proportion of PS points with deformation rates greater than $\pm$ 3 mm/a reached 7.2% and 7.6% along Line 5 and the PJ Line, respectively, while these proportions were much lower along the other lines.

(3) The variations in the land subsidence trend along the subway lines around the time they opened to traffic indicated that subway construction played a great role during the land subsidence process. These clear descriptions of the deformation characteristics changes over such a long period were unprecedented. The land subsidence and groundwater level maintained a significantly positive correlation, leading to microscale ground deformation (settlement or rebound) as the groundwater level rose.

Although the land subsidence in Shanghai has entered a stage of microscale deformation, the surrounding engineering construction projects, such as human-induced ground loading, foundation pit construction, and road construction, have become the main factors affecting local land subsidence intensification along the subway lines, and these factors need to be given great attention for the prevention and control of land subsidence.

Author Contributions: Methodology, formal analysis, writing—original draft preparation: J.Z. and X.S.; writing—review and editing: J.L. and R.W.; supervision: C.K. All authors have read and agreed to the published version of the manuscript.

Funding: This research was funded by Natural Science Foundation of Jiangsu Province, grant number BK20210193, and a project supported by the Science and Technology Commission of Shanghai Municipality, grant numbers 20DZ1201200,21DZ1204201, 19DZ1200902, and 22ZR1447100.

Data Availability Statement: Not applicable.

Acknowledgments: We would like to thank the Shanghai Institute of Geological Survey for providing geological environment data, the Shanghai Surveying and Mapping Institute for providing optical images, and the German Aerospace Center for providing the TerraSAR data used in this study.

Conflicts of Interest: The authors declare no conflict of interest.

References

1. Bagheri-Gavkosh, M.; Bagheri, M.; Hosseini, S.M.; Ataie-Ashtiani, B.; Sohani, Y.; Homa Ebrahimian, H.; Morovat, F.; Ashrafi, S. Land Subsidence: A Global Challenge. *Sci. Total Environ.* **2021**, *778*, 146–193. [CrossRef] [PubMed]
2. Faunt, C.C.; Sneed, M.; Traum, J.; Brandt, J.T. Water Availability and Land Subsidence in the Central Valley, California, USA. *Hydrogeol. J.* **2016**, *24*, 675–684. [CrossRef]
3. Yan, X.X.; Yang, T.L. Suggestions for a Strategy on Land Subsidence Prevention and Control in Shanghai Under the New Situation. *Shanghai Land Resour.* **2020**, *41*, 5–6.
4. Ge, D.Q. *Research on the Key Techniques of SAR Interferometry for Regional Land Subsidence Monitoring*; China University of Geosciences: Beijing, China, 2013.
5. Lin, J.X. Comparative Study on Development Background of Land Subsidence Between Shanghai, China and Hanoi, Vietnam. *Shanghai Land Resour.* **2022**, *43*, 84–88.
6. Bao, S.K.; Ye, S.J.; Yan, X.X.; Yang, T.L.; Huang, X.L. Subsidence Characteristics, Groundwater Pumping, and Recharge of Land Subsidence Prevention and Control Zone in Shanghai. *Shanghai Land Resour.* **2021**, *42*, 1–7.
7. Gezgin, C. The Influence of Ggroundwater Levels on Land Subsidence in Karaman (Turkey) Using the PS-InSAR Technique. *Adv. Space Res.* **2022**, *70*, 3568–3581. [CrossRef]
8. Rahmati, O.; Golkarian, A.; Biggs, T.; Keesstra, S.; Mohammadi, F.; Daliakopoulos, I.N. Land Subsidence Hazard Modeling: Machine Learning to Identify Predictors and the Role of Human Activities. *Environ. Manag.* **2019**, *236*, 466–480. [CrossRef]
9. Pu, C.H.; Xu, Q.; Zhao, K.Y.; Chen, W.L.; Wang, X.C.; Li, H.J.; Liu, J.L.; Kou, P.L. Spatiotemporal Evolution and Surface Response of Land Subsidence over a Large-scale Land Creation Area on the Chinese Loess Plateau. *Int. J. Appl. Earth Obs. Geoinf.* **2022**, *111*, 102835. [CrossRef]
10. Nguyen, Q.T. The Main Causes of Land Subsidence in Ho Chi Minh City. *Procedia Eng.* **2016**, *142*, 334–341. [CrossRef]
11. Ventura, G.; Vilardo, G.; Terranova, C. Multiple Causes of Ground Deformation in the Napoli Metropolitan Area (Italy) from Integrated Persistent Scatterers DinSAR, Geological, Hydrological, and Urban Infrastructure Data. *Earth-Sci. Rev. Int. Geol. J. Bridg. Gap Res. Artic. Textb.* **2015**, *146*, 105–119.
12. Ding, P.P.; Jia, C.; Di, S.T.; Wu, J.; Wei, R.C. Analysis and Evaluation of Land Subsidence along Linear Engineering Based on InSAR Data. *KSCE J. Civ. Eng.* **2021**, *25*, 3477–3491. [CrossRef]
13. Sun, H.; Zhang, Q.; Zhao, C.Y.; Yang, C.S.; Sun, Q.F.; Chen, W.R. Monitoring Land Subsidence in the Southern Part of the Lower Liaohe Plain, China with a Multi-track PS-InSAR Technique. *Remote Sens. Environ.* **2017**, *188*, 73–84. [CrossRef]
14. Yang, T.L.; Xu, Y. Research Ttrends in internationnal Land Subsidence and Urban Security: An Overview of the First International Symposium on Urban Geology. *Shanghai Land Resour.* **2017**, *38*, 1–3.
15. Zhang, A.G.; Wei, Z.X. Past, Present and Future Research on Land Subsidence in Shanghai City. *Hydrogeol. Eng. Geol.* **2002**, *5*, 72–75.
16. Gong, S.L. Review on Land Subsidence Research of Shanghai. *Shanghai Geogloy* **2006**, *27*, 25–29.
17. Jiao, X.; Wang, H.M.; Yang, T.L.; Fang, Z.; Lin, J.X.; Zhang, H. Regionalization of Land Subsidence Prevention Based on the Consideration of Uncontrollable Factors. *Shanghai Land Resour.* **2017**, *38*, 4–8.
18. Zhou, L.; Li, J.H.; Wang, C.; Li, S.; Zhu, Z.L.; Lv, J.J. Analysis of Time-series InSAR-based Subsidence Monitoring along the 2018-2020 Metro Line in Shanghai Area. *Geod. Geodyn.* **2021**, *41*, 1177–1182.
19. Zhu, J.J.; Li, Z.W.; Hu, J. Research Progress and Methods of InSAR for Ddeformation Monitoring. *Acta Geod. Cartogr. Sin.* **2017**, *46*, 1717–1733.
20. Liao, M.S.; Wang, R.; Yang, S.M.; Wang, N.; Qin, X.Q.; Yang, T.L. Techniques and Applications of Spaceborne Time-series InSAR in Urban Dynamic Monitoring. *J. Radars* **2020**, *9*, 409–424.
21. Yao, G.H.; Ke, C.Q.; Zhang, J.H.; Lu, Y.Y.; Zhao, J.M.; Lee, H. Surface Deformation Monitoring of Shanghai Based on ENVISAT ASAR and Sentinel-1A Data. *Environ. Earth Sci.* **2019**, *78*, 225. [CrossRef]
22. Yang, M.S.; Wang, R.; Li, M.H.; Liao, M.S. A PSI Targets Characterization Approach to Interpreting Surface Displacement Signals: A Case Study of the Shanghai Metro Tunnels. *Remote Sens. Environ.* **2022**, *280*, 113150. [CrossRef]
23. Lin, H.; Ma, P.F.; Wang, W.X. Urban Infrastructure Health Monitoring with Spaceborne Multi-temporal Synthetic Aperture Radar Interferometry. *Acta Geod. Cartogr. Sin.* **2017**, *46*, 1421–1433.
24. Qiu, Y.H.; Bie, W.P.; Bo, Z.Y.; Li, C.Q.; Zheng, K.; Lang, B. Urban Underground Rail Transit Subsidence and Disaster Monitoring Based on InSAR. *Bull. Surv. Mapp.* **2020**, *2*, 107–112.
25. Barla, G.; Tamburini, A.; Conte, S.D.; Giannico, C. InSAR Monitoring of Tunnel Induced Ground Movements. *Geomech. Tunn.* **2016**, *9*, 15–22. [CrossRef]
26. Fang, Z.L.; Wang, H.M.; Wu, J.Z.; Lu, L.J.; Wang, Y. Application Research on Monitoring Land Subsidence Research in Shanghai Using InSAR Technology. *Shanghai Geogloy* **2009**, *2*, 22–26.
27. Wang, R.; Yang, M.S.; Dong, J.; Liao, M.S. Investigating Deformation Along Metro Lines in Coastal Cities Considering Dfferent Structures With InSAR and SBM Analyses. *Int. J. Appl. Earth Obs. Geoinf.* **2022**, *115*, 103099.
28. Zhang, C.S.; Zhu, J.J.; Hu, J.; Wang, X.W. Study on Two Pass D-InSAR Using SRTM Data for Urban Land Subsidence Measurement. *Sci. Surv. Mapp.* **2009**, *34*, 45–47.
29. Wan, Y.; Liao, M.S.; Li, D.R.; Wei, Z.X.; Fang, Z. Subsidence Velocity Retrieval from Long-term Coherent Targets in Radar Interferometric Stacks. *Chin. J. Geophys.* **2007**, *50*, 598–604.

30. Yang, M.S.; Jiang, Y.N.; Liao, M.S.; Wang, H.M. The Analysis of the Subsidence Patterns in Lingang New City (Shanghai) Using High-resolution SAR images. *Shanghai Land Resour.* **2013**, *34*, 12–16.
31. Qin, X.Q.; Yang, M.S.; Wang, H.M.; Yang, T.L.; Lin, J.X.; Liao, M.S. Exploring Temporal-Spatial Characteristics of Shanghai Road Networks Subsidence with Multi-temporal PS-InSAR Technique. *Acta Geod. Cartogr. Sin.* **2016**, *45*, 713–721.
32. Hooper, A.; Segall, P.; Zebker, H. Persistent scatterer interferometric synthetic aperture radar for crustal deformation analysis, with application to Volcán Alcedo. *J. Geophys. Res.* **2007**, *112*, 763. [CrossRef]
33. Qin, X.Q.; Yang, T.L.; Yang, M.S.; Zhang, L.; Liao, M.S. Health Diagnosis of Major Transportation Infrastructures in Shanghai Metropolis Using High-Resolution Persistent Scatterer Interferometry. *Sensors* **2017**, *17*, 2270. [CrossRef]
34. Dai, K.; Liu, G.; Li, Z.; Li, T.; Yu, B.; Wang, X.; Singleton, A. Extracting Vertical Displacement Rates in Shanghai (China) with Multi-Platform SAR Images. *Remote Sens.* **2015**, *7*, 9542–9562. [CrossRef]
35. Zhao, Q.; Ma, G.; Wang, Q.; Yang, T.L.; Liu, M.; Gao, W.; Falabella, F.; Mastro, P.; Pepe, A. Generation of Long-term InSAR Ground Displacement Time-series Through a Novel Multi-sensor Data Merging Technique: The Case Study of the Shanghai Coastal Area. *ISPRS J. Photogramm. Remote Sens.* **2019**, *154*, 10–27. [CrossRef]
36. Wei, Z.X.; Zhai, G.Y.; Yan, X.X. *Shanghai Urban Geology*; Geology Press: Beijing, China, 2010.
37. Jin, Y.; Zi, H.B. Explorations and Practices of Rail Transit Multi-level network Integration Planning in Shanghai. *J. Transp. Eng.* **2020**, *5*, 7–13.
38. Ni, W.P.; Bian, H.; Yan, W.D.; Zheng, G.; Lv, Y. System Characteristics and Application Analysis of TerraSAR-X Radar Satellite. *Radar Sci. Technol.* **2009**, *7*, 29–34.
39. Ferreti, A.; Prati, C.; Rocca, F. Permanent Scatterers in SAR Interferometry. *J. Traps. Geosci. Remote Sens.* **2001**, *39*, 8–20. [CrossRef]
40. Liao, M.S.; Wang, T. *Time-Series InSAR Technology and Application*; Science Press: Beijing, China, 2014.
41. Shi, H.Y. *Research on Regional Subsidence Monitoring along High-Speed Railway Using MT-InSAR Technique*; Beijing Jiaotong University: Beijing, China, 2013.
42. Li, J.; Zhou, L.; Zhu, Z.; Qin, J.; Xian, L.; Zhang, D.; Huang, L. Surface Deformation Mechanism Analysis in Shanghai Areas Based on TS-InSAR Technology. *Remote Sens.* **2022**, *14*, 4368. [CrossRef]
43. Chen, Y.; Liao, M.; Wu, J.; Li, X.; Xiong, F.; Liu, S.; Feng, Y.; Wang, X. Elastic and Inelastic Ground Deformation in Shanghai Lingang Area Revealed by Sentinel-1, Leveling, and Groundwater Level Data. *Remote Sens.* **2022**, *14*, 2693. [CrossRef]
44. Hu, C.L.; Li, L.Z.; Zhu, H.F.; Kong, Y.; Hu, X.F. *Shanghai Water Resources Bulletin in 2020*; Shanghai Water Authority: Shanghai China, 2020.